A&A 373, 199–210 (2001)
DOI: 10.1051/0004-6361:20010594

Astronomy & Astrophysics

Doppler imaging of stellar surface structure

XVI. A time-series analysis of the moderately-rotating K1-giant σ Geminorum

Zs. Kővári[1], K. G. Strassmeier[2,⋆], J. Bartus[1], A. Washuettl[2,⋆], M. Weber[2,⋆], and J. B. Rice[3]

[1] Konkoly Observatory of the Hungarian Academy of Sciences, 1525 Budapest, Hungary
e-mail: kovari@konkoly.hu; bartus@konkoly.hu
[2] Astrophysikalisches Institut Potsdam, An der Sternwarte 16, 14482 Potsdam, Germany
e-mail: kstrassmeier, wasi, mweber@aip.de
[3] Department of Physics, Brandon University, Brandon, Manitoba R7A 6A9, Canada
e-mail: rice@BrandonU.ca

Received 9 June 2000 / Accepted 24 April 2001

Abstract. We present a simultaneous photometric and spectroscopic imaging analysis of the long-period RS CVn binary σ Gem, covering 3.6 consecutive rotation cycles with high time resolution. From six overlapping but consecutive Doppler maps we trace the evolution of individual spots throughout the time range covered. All spots group either along a band at approximately +45° latitude and a width of 30°, or appear centered at the equator. No polar spot is detected. We did not find a conclusive migration pattern from the cross-correlation maps from one rotation to the next and attribute this to a masking effect of short-term spot changes.

Key words. stars: activity – stars: imaging – stars: individual: σ Gem – stars: late-type – starspots

1. Introduction

σ Geminorum (75 Gem, HR 2973, HD 62044) is a bright and moderately-rotating K1 giant in a long-period RS CVn-type binary (Linsky 1984) with $V \approx 4\overset{\mathrm{m}}{.}15$ and $P_{\rm rot} \approx P_{\rm orb} \approx 20$ days. The photometric light variation is due to spots on the K1III primary component. The secondary component is probably a cool main-sequence star of G or K spectral type (Ayres et al. 1984) but is not seen in the optical spectrum nor in the photometry.

The system shows all signs of solar-like magnetic activity. σ Gem is included in the *Catalog of Chromospherically Active Binary Stars* (Strassmeier et al. 1993, hereafter CABS II) because of its strong Ca II H&K emission originally discovered by Eberhard & Schwarzschild (1913). From early IUE observations in the far UV, Ayres et al. (1984) reported the presence of center-to-limb modulation effects in the spectra. This was further strenghtened by the finding that the Hα core emission also varied with the rotational phase (Eker 1986; Bopp et al. 1988) and thus established the star's chromospheric activity due to plage-like regions. The soft X-ray emission also showed such rotational modulation, as reported by Engvold et al. (1988) and Singh et al. (1987), which even suggests an inhomogeneous active corona. Long-term cyclic variation with a probable period of 8.5 years was found by Henry et al. (1995) who analyzed the ≈16 years long photometric history of σ Gem. Variations on time scales from hours to years were detected in the ROSAT PSPC bandpass by Yi et al. (1997). Furthermore, σ Gem is long known as a radio source (Spangler et al. 1977; Gibson 1980, CABS II and references therein).

Orbital and rotational period determinations (Strassmeier et al. 1988; Henry et al. 1995; Jetsu 1996; Strassmeier et al. 1999a) obtained very similar values differing by less than 1%. Updated orbital elements were obtained by Bopp & Dempsey (1989), and recently by Dümmler et al. (1997) who concluded, that the secondary component could be a compact object or, alternatively, the primary is not a normal K1III star. Assuming a circular orbit, an orbital period of 19.604 days was determined by Dümmler et al. (1997). The optical spectral lines are rotationally broadened by $v \sin i = 27 \pm 2$ km s^{-1} (Eaton 1990). Dümmler et al. (1997) found the same value and also argued for $\log g = 2.5$ as the most likely gravity in agreement with canonical values for K giants listed, e.g. in Gray (1992).

The detailed photometric studies with starspot-modelling techniques by Fried et al. (1983),

Send offprint requests to: K. G. Strassmeier,
e-mail: kstrassmeier@aip.de

⋆ Visiting Astronomer, National Solar Observatory, operated by the Association of Universities for Research in Astronomy, Inc. under contract with the National Science Foundation.

Strassmeier et al. (1988), Oláh et al. (1989), Dempsey et al. (1992), Henry et al. (1995), and, more recently, Jetsu (1996) and Berdyugina & Tuominen (1998) found the presence of at least two long-living large active regions (spots) on the primary. These studies are qualitatively in agreement with Eker's (1986) early spectroscopic study, where an estimation of the inclination angle of $45° \leq i \leq 73°$ was also given.

Finally, Hatzes (1993) presented the first Doppler image of σ Gem and found five spots in a band centered at a medium latitude which he interpreted as an active-latitude belt. No evidence of a polar cap-like spot was seen. The $v \sin i$ of 27 km s^{-1} and the inclination of $i = 60°$ adopted by Hatzes (1993) yield a radius of $\approx$12 $R_\odot$, which is consistent with a spectral type of a normal K1III giant.

The present paper is the 16th paper in our series of stellar surface structure. The aim of this series is to find evidence for systematic changes of the surface temperature distribution that are related to basic astrophysical parameters like age, mass, and rotation, and to detect specific surface phenomena like differential rotation or meridional flows. In this paper, we present a Doppler-imaging analysis with new high-resolution spectra and *by* photometry that covered 3.6 consecutive stellar rotations of σ Gem.

2. Observations

2.1. Spectroscopy

All spectroscopic observations were obtained with the McMath-Pierce telescope at Kitt Peak National Solar Observatory (NSO). Our 52 spectra were taken during a 70 nights long observing run between 1 November 1996−9 January 1997, covering 3.57 consecutive stellar rotations. We used the stellar spectrograph with the 800×800 TI-4 CCD camera at a dispersion of 0.10 Å/pixel and a resolving power of 42 000 as judged from the width of several Th-Ar comparison-lamp lines. The observations covered the 6410–6460 Å wavelength range but include only two lines suitable for Doppler imaging (Ca I 6439 and Fe I 6430) due to a cosmetic defect on the detector. The average signal-to-noise (S/N) ratio is $\approx$400:1 but many spectra have more than 500:1 and several also near 300:1.

Data reductions were done using the NOAO/IRAF software package and followed our standard procedure for coudé spectra (see, e.g., Weber & Strassmeier 1998). Nightly observations of the radial-velocity standard α Ari were used to obtain the radial velocities for σ Gem, except for one night where β Gem was used instead. We adopted $v_{\alpha\mathrm{Ari}} = -14.51$ km s^{-1} and $v_{\beta\mathrm{Gem}} = +3.23$ km s^{-1} (Scarfe et al. 1990). Table 1 gives the observing log and the radial velocities.

Our data are phased with the orbital period from Dümmler et al. (1997) and from a recent time of maximum positive velocity according to our Table 1

$$\mathrm{HJD} = 2\,450\,388.36853 + 19.60447 \times E. \quad (1)$$

Table 1. Observing log and radial velocities.

HJD (2 400 000+)	phase (Eq. (1))	v_r (km s^{-1})	σ_vr (km s^{-1})
50389.017	0.033	76.4	1.2
50391.024	0.135	64.1	1.3
50391.920	0.181	59.6	1.7
50392.885	0.230	43.4	1.4
50393.875	0.281	40.6	1.5
50394.838	0.330	27.9	0.7
50395.899	0.384	16.9	1.4
50396.895	0.435	9.4	1.8
50399.057	0.545	7.6	1.4
50400.004	0.594	15.2	1.5
50400.993	0.644	23.8	0.9
50401.988	0.695	34.8	1.4
50404.938[a]	0.845	60.8	1.9
50405.862[a]	0.892	66.7	2.1
50406.942[a]	0.947	75.8	1.5
50408.886[a]	1.047	77.9	1.7
50411.960	1.203	55.2	1.7
50412.945	1.254	42.8	1.3
50415.893	1.404	15.2	1.4
50416.864	1.454	9.4	1.2
50417.952	1.509	9.4	1.1
50418.949	1.560	12.0	1.7
50419.890	1.608	16.8	1.4
50420.931	1.661	25.1	1.5
50421.926	1.712	35.2	1.9
50422.912	1.762	45.6	1.7
50423.880	1.811	55.3	1.7
50424.999	1.869	66.1	1.6
50425.980	1.919	75.2	1.5
50426.985	1.970	78.7	1.8
50428.959	2.071	75.0	1.6
50429.973	2.122	68.9	1.4
50430.972	2.173	61.8	1.7
50431.846	2.218	48.4	1.4
50432.878	2.270	38.4	1.9
50433.841	2.320	28.7	1.6
50434.898	2.373	19.2	1.4
50435.934	2.426	13.1	1.3
50436.913	2.476	7.8	1.2
50437.868	2.525	10.2	1.2
50438.833	2.574	14.7	1.2
50439.923	2.630	19.3	1.7
50440.865	2.678	26.4	1.7
50441.942	2.733	41.2	1.9
50444.893[b]	2.883	68.0	2.2
50446.900	2.986	78.7	2.6
50447.914	3.037	77.2	1.5
50450.015	3.145	65.7	1.9
50450.937	3.192	57.1	1.3
50451.926	3.242	46.6	1.8
50456.902	3.496	9.0	1.5
50457.896	3.547	12.0	1.3

[a] Nights where no radial-velocity standard was observed. These velocities rely on a zeropoint from the Th-Ar comparison lamp.
[b] β Gem was measured as v_r standard.

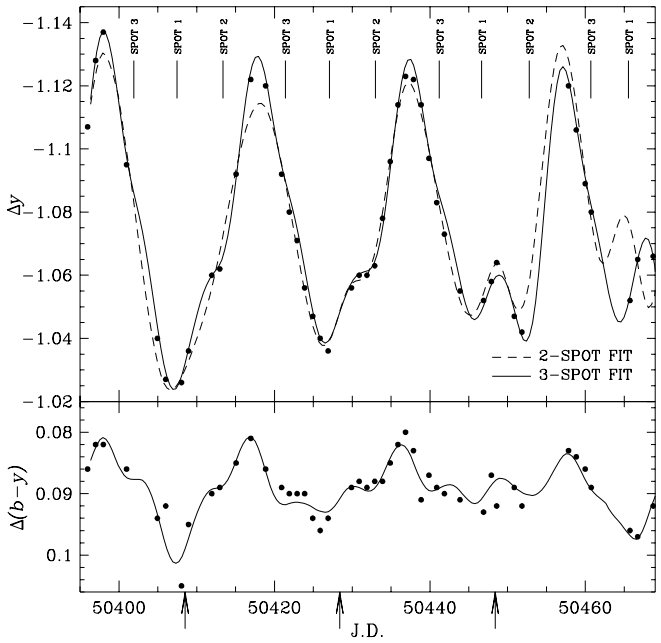

Fig. 1. Photometric light variations of σ Gem between 8 November 1996–21 January 1997 in the Δy band and $\Delta(b-y)$ colour. The upper panel shows the y data and the result of our time-series photometric spot modelling using either a two-spot (dashed line) or a three-spot assumption (solid line). The lower panel displays the colour curve and the fit obtained using a spot temperature of 600 K cooler than the photospheric background temperature.

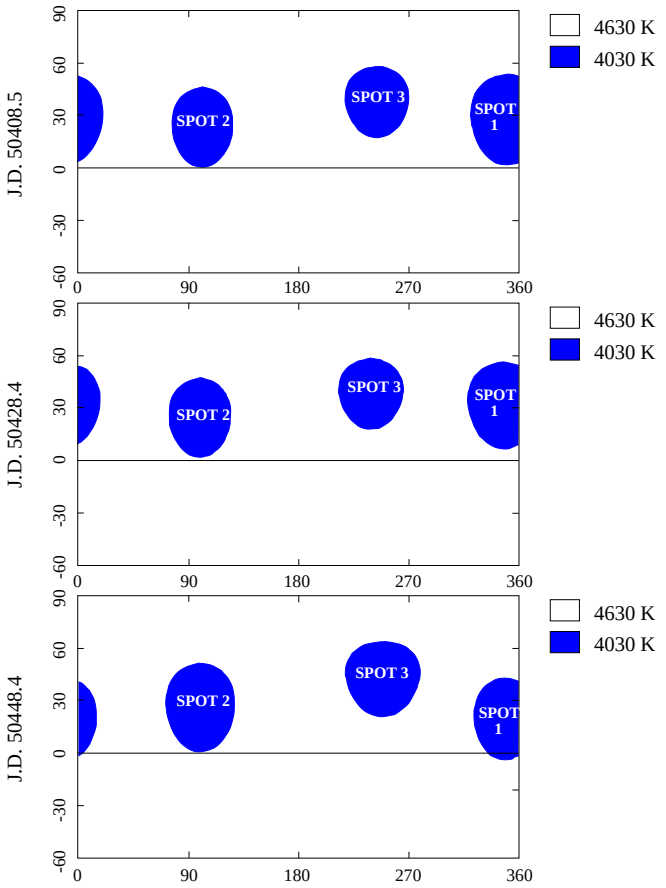

Fig. 2. Mercator plots of the time-series spot modelling at three different epochs. Shown are the times marked by the three arrows on the time-axis in Fig. 1. For more explanations see the text.

2.2. Photometry

Photometric data were collected between 8 November 1996−21 January 1997 with the Wolfgang 0.75-m automatic photoelectric telescope (APT) of the University of Vienna and located at Fairborn Observatory in Arizona (Strassmeier et al. 1997). The telescope was equipped with Strömgren b and y filters. Altogether, 46 new by measurements were obtained during the spectroscopic campaign, each of them being the mean of eight readings per night on average. HD 60318 was used as the comparison star (Hipparcos magnitudes of HD 60318 are $V = 5\overset{\mathrm{m}}{.}34$, $B-V = 1\overset{\mathrm{m}}{.}010$, $V-I = 0\overset{\mathrm{m}}{.}99$; ESA 1997).

3. Time-series light curve analysis

3.1. The light-curve modelling code

For the spot modelling, we apply the TISMO code developed by Bartus (1996) and sucessfully applied to the RS CVn binary HR 1099 in Strassmeier & Bartus (2000). The code is written for inverting the light curve variations in the time domain rather in the (rotational) phase domain. It is thus able to provide a continuous fit for the photometric light variations in consecutive rotational cycles caused by starspots with varying geometry. The output parameters are the time dependent spot coordinates. By assuming circular dark spots these are the spot longitudes ($\lambda_i(t)$), the spot latitudes ($\beta_i(t)$), and the spot radii ($\gamma_i(t)$). Errors are estimated according to the photometric precision of the data and the procedure described in Bartus (1996).

Because the secondary component is not seen, the photometric variations are attributed entirely to the K1III primary component. For the modelling, two a priori assumptions are made. First, the surface temperature is fixed to $T_{\rm phot} = 4630$ K (cf., Sect. 4.2) and second, the "unspotted" brightness level remains fixed at the maximum brightness ever observed, i.e $V_{\rm max} = 4\overset{\mathrm{m}}{.}137$ (cf. Strassmeier et al. 1988). The inclination of the stellar rotation axis was set to the most probable value of $i = 60°$ (cf., Sect. 4.2 and Eker 1986).

3.2. Results

We started the modelling with just two spots but after a few runs it became clear that the number of spots had to be increased to three to obtain a satisfactory fit to the light curve (Fig. 1). Having the spot temperature as a free parameter, we fit the $b-y$ curve to search for the most probable spot temperature. Fits are obtained for spot temperatures cooler than the surrounding photosphere of 200 K−900 K in steps of 100 K. The best fit was

obtained using $\Delta T_{\rm spot} = 600 \pm 100$ K, i.e., $T_{\rm spot} \approx 4030$ K. The upper panel of Fig. 1 shows the y-band data and the model fits with either two or three spots with this temperature, while the lower panel shows the model fit for $b-y$ with just the three-spot case.

We find that the three spots are nearly equally spaced in longitude, as indicated in the upper bars in Fig. 1, and also illustrated in Fig. 2. The latter figure shows mercator plots of the three-spot solution at three different epochs following each other by one rotational cycle (these epochs coincide with the mid-epochs of the spectroscopic datasets SS2, SS4 and SS6, respectively, used later in Sect. 4). The spot areas are also comparable, between 20°–30° in radii. The total spot coverage varies thus between 10–20% of a hemisphere during one rotation. Despite that the spot latitudes are the most uncertain parameters, the resulting latitudinal positions indicate spottedness predominantly at lower latitudes. In our solutions, cool regions do not reach latitudes higher than ≈60°.

Considerable evolution of the spot parameters is not seen, however, a small systematic decrease of the longitudes of SPOT 1 and SPOT 2 is present, while SPOT 3 performs a mixed motion with replacements in both directions and also an increase in size. The spot migrations are of the order of 2–3° per rotational cycle, i.e. the order of the uncertainty of the spot modelling (see, e.g., Kővári & Bartus 1997). Thus, the detection of such small spot-motion patterns and their interpretation due to surface differential rotation requires longer baselines in time.

4. Time-series Doppler imaging analysis

We prepared six data subsets (SS1–SS6) out of the 70-day long spectroscopic coverage. Each subset covers approximately one rotation period separated by half a rotation. The successive subsets thus overlap by approximately half of a rotation period but subsets 1, 3, and 5, as well as 2, 4, and 6 represent contiguous stellar rotations. The mid Julian dates for the individual subsets SS1–SS6 are 2 450 397.980, 2 450 408.505, 2 450 417.935, 2 450 428.410, 2 450 438.435 and 2 450 448.365, respectively. Each spectroscopic dataset is supported by simultaneous photometric observations.

4.1. The line profile inversion code

Our line-profile inversion code performs a full LTE spectrum synthesis by solving the equation of transfer through a set of Kurucz (1993) model atmospheres, at all aspect angles, and for a given set of chemical abundances. Simultaneous inversions of eight spectral lines, as well as two photometric bandpasses, were carried out using a maximum-entropy regularisation. The number of iterations was set to 15 which proved to be sufficient for a good convergence. The computations were performed on a Sun Ultra-2 workstation at Konkoly Observatory and required 20–30 min of CPU time for each Doppler map. A more detailed description of the TempMap code and additional references regarding our line-profile inversion technique can be found in Rice et al. (1989) and Piskunov & Rice (1993) and previous papers of this series (e.g., Rice & Strassmeier 1998; Strassmeier & Rice 1998).

Table 2. Astrophysical data for σ Gem.

Parameter	Value
Classification	K1 III
Distance (Hipparcos)	37.5 ± 1.1 pc
Luminosity, L	$52.5^{+14.5}_{-8.2}$ $L_\odot$
$\log g$	$2.5^{+0.23}_{-0.42}$
$T_{\rm eff}$	4630 ± 100 K
$(B-V)_{\rm Hipparcos}$	1.118 ± 0.006 mag
$(V-I)_{\rm Hipparcos}$	1.12 ± 0.05 mag
$v \sin i$	27.5 ± 1 km s^{-1}
Inclination, i	$60° \pm 15°$
Period, $P_{\rm rot} = P_{\rm orb}$	19.60447 ± 0.00007 days
Orbital eccentricity, e	0.0
Radius, R	$12.3^{+1.6}_{-1.0} R_\odot$
Microturbulence for Ca, $\xi_{\rm Ca}$	0.7 km s^{-1}
Microturbulence for Fe, $\xi_{\rm Fe}$	1.0 km s^{-1}
Macroturbulence, $\zeta_{\rm R} = \zeta_{\rm T}$	3.0 km s^{-1}
Chemical abundances	solar (adopted)

Table 3. Adopted atomic line parameters.

Element	Ion	λ (Å)	$\log gf$	$\chi_{\rm low}$ (eV)
Eu	II	6437.640	–0.45	1.320
Si	I	6437.703	–2.35	5.863
Ni	I	6437.992	–0.75	5.389
V	I	6438.088	+0.25	2.684
Fe	I	6438.755	–2.48	4.435
Ca	I	**6439.075**	**+0.10**	**2.526**
Fe	I	6439.554	–3.05	4.473
Si	I	6440.566	–2.48	5.616
Fe	I	6429.071	–3.41	4.294
Co	I	6429.906	–2.41	2.137
V	I	6430.472	–1.00	1.955
Fe	I	**6430.844**	**–2.00**	**2.176**
Ca	I	6431.099	–2.61	3.910
V	I	6431.623	–1.25	1.950
Ni	I	6431.994	–1.75	3.542
Fe	II	6432.680	–3.74	2.891

4.2. Astrophysical input

Table 2 summarizes the astrophysical input parameters for σ Gem. We adopt $i = 60°$ as the most likely inclination angle. This value was determined by reducing the misfit of the line profiles as a function of the inclination (for the method see, e.g., Rice & Strassmeier 2000 a.o.). Its uncertainty is estimated from the width of the χ^2 minimum and is approximately ±15°.

Our best value for the projected rotational velocity, $v_{\rm eq} \sin i$, was determined by minimizing the artificial dark or bright bands in the Doppler maps that appear if the equatorial velocity, $v_{\rm eq}$, is either too large or too small,

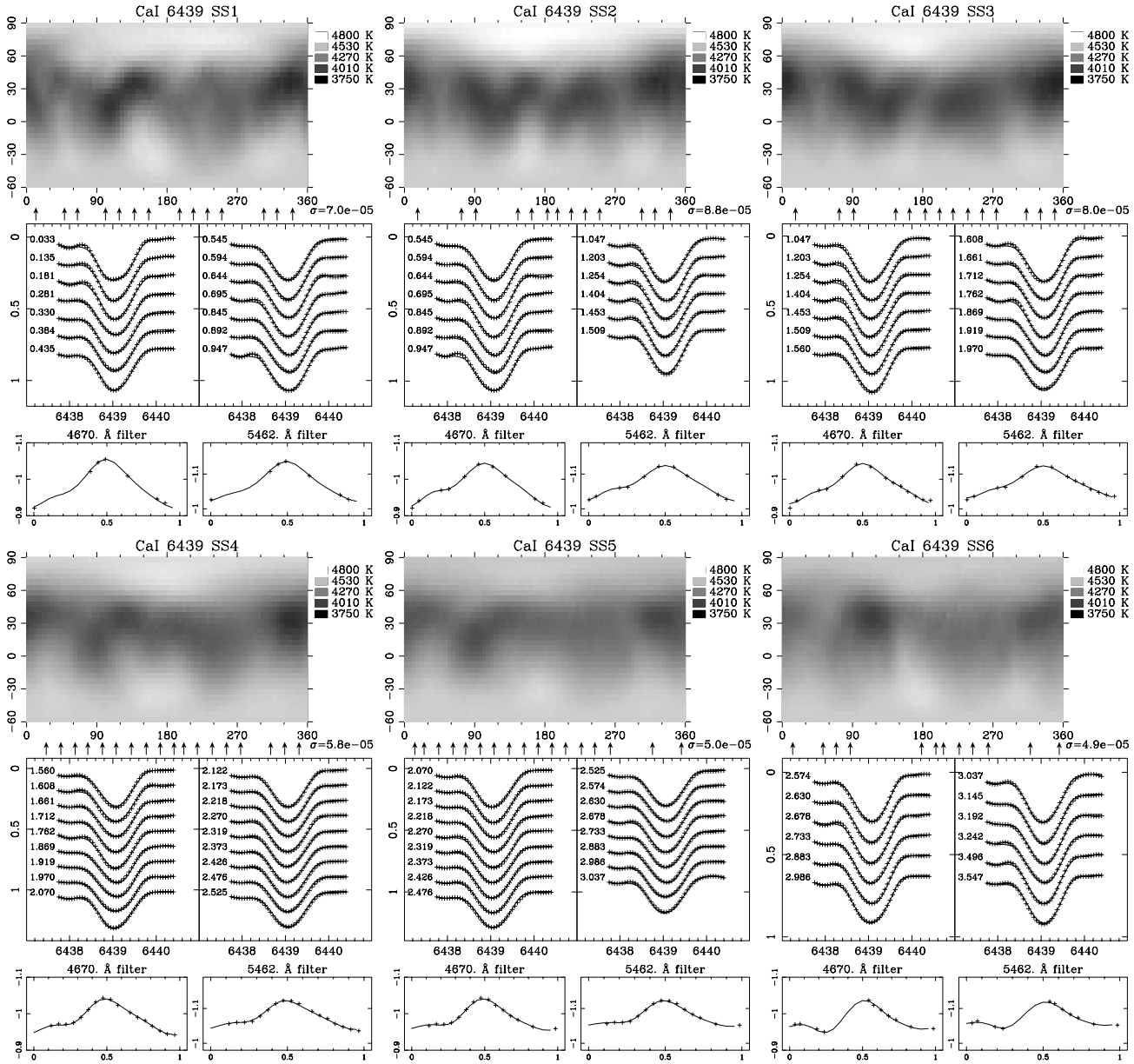

Fig. 3. Ca I 6439-Å images for the six subsets SS1–SS6. The maps are presented in a pseudo-Mercator projection from latitude $-60°$ to $+90°$. The line profiles and their fits are shown in the middle row, the light curves and their respective fits are plotted in the bottom two rows for the Strömgren b and y bands, respectively. The phases of the observations are marked by arrows below the maps.

respectively (for more details see, e.g., Strassmeier et al. 1998, 1999b). Its uncertainty depends on the S/N ratio and on the "external quality" of the spectra (i.e. wavelength calibration, flat fielding, etc.) but also whether we have a low-gravity giant atmosphere or a high-gravity dwarf atmosphere and, last but not least, on the spot morphology on the stellar surface. In case of the K1 giant σ Gem, we estimate an uncertainty of ± 1 km s^{-1}.

The minimum radius is computed from the assumption that the rotation is synchronized to the orbital motion. $R \sin i$ becomes then 10.65 ± 0.35 $R_\odot$ and, with $i = 60° \pm 15°$, $R \approx 12.3^{+3.2}_{-1.6}$ $R_\odot$. This value is formally below the lower bound of radii found in the literature for K1 giants (e.g. Gray 1992). The Hipparcos parallax of 26.70 ± 0.79 milli-$''$ (ESA 1997) and the brightest V magnitude observed so far, $V = 4\overset{\text{m}}{.}137$ (see Sect. 3), result in an absolute visual brightness of $+1\overset{\text{m}}{.}27$ which is almost one magnitude fainter than tabulated values for K1 giants (Gray 1992). The radius from the Hipparcos distance and the effective temperature of 4630 K is 9.3 $R_\odot$ (with $B.C. = -0.515$; Flower 1996), and is also much smaller than for a fully developed K1 giant and even smaller than our measured minimum radius $R \sin i$. However, adopting the average surface temperature of ≈4200 K from our Doppler images as the effective temperature, the radii agree to within their uncertainties. O'Neil et al. (1996) obtained a photospheric temperature of 4500 K and an average spot temperature of 3850 K from measuring

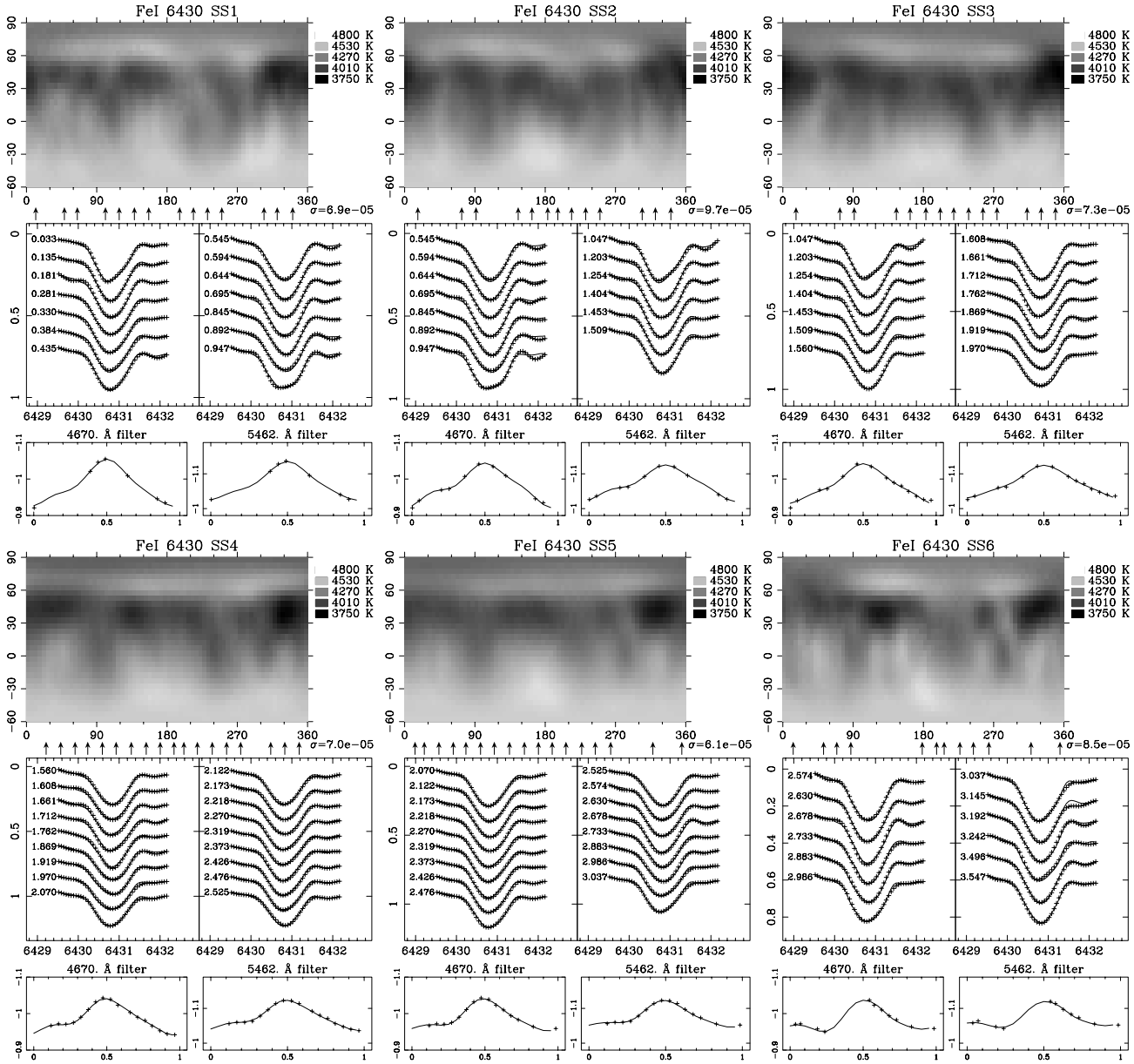

Fig. 4. Fe I 6430-Å images for the six subsets SS1–SS6. Otherwise as in Fig. 3.

titanium oxide bands contemporaneous with BV photometry. The Hipparcos $B-V$ of 1.118 indicates 4630 K (according to the calibration of Flower 1996). In any case, this temperature and the bolometric magnitude of $+0\overset{\mathrm{m}}{.}75$ suggests that σ Gem is beyond the base of the giant branch but not yet in the helium core-burning phase. A comparison with the evolutionary tracks from Schaller et al. (1992) for solar metallicity implies a mass of $1.5 \pm 0.2\ M_{\odot}$ and an approximate age of 2.8 Gyr.

4.3. Atomic line-data input

In this study, we use the Ca I line at 6439 Å and the Fe I line at 6430 Å as the main mapping lines. In the (photospheric) temperature range for σ Gem, the Ca I-6439 line is quite temperature sensitive. Therefore, cooler regions on the stellar surface will appear less pronounced because inside the spot, i.e. in the regions with lesser continuum intensity, the Ca line has a relatively large equivalent width and hence the bump produced by the spot in the Ca profiles appears less significant. As a result, the Ca I-6439 images provide inferior "resolution" compared to the Fe I-6430 images. The iron line has the advantage that it is less sensitive to the surface temperature gradient and thus has a smaller equivalent width compared to the Ca line. Its Doppler images provide thus more surface detail. However, better fits in the sense of lower χ^2 are obtained for the Ca spectra. Unfortunately, Fe I-6430 is blended by several relatively strong metal lines, most notably Fe II at 6432 Å.

In Table 3, we summarize the atomic parameters that we adopted for the Ca I-6439 and the Fe I-6430 spectral

regions. By default, solar photospheric abundances were assumed which required alteration of some of the $\log gf$ values from the line list of Kurucz (1993) in order to obtain better fits to the spectra. The effect of an abundance change on the line-profile reconstruction is not distinguishable from a change of $\log gf$, as was noted in previous papers in this series and quantified in tests with artificial data by Rice & Strassmeier (2000). Also, abundances from just a single spectral line can be notoriously uncertain and we chose not to solve for the abundance but adjust the transition probability instead.

4.4. Doppler images for 1996/97

Figures 3 and 4 show the results for the Ca I-6439 and the Fe I-6430 line region, respectively. Six (overlapping) maps for each wavelength region are obtained (SS1–SS6). None of the maps recovered a polar cap-like spot, nor any other spots at latitudes higher than 60°. Spots were found mainly along a belt between 30° and 60° latitude, but some weaker features were recovered in the low-latitude regions ±30° from the equator. The main features in the medium-latitude belt have temperature contrasts of $\Delta T = T_{\rm phot} - T_{\rm spot} \approx 800$ K from the Fe map and 700 K from the Ca map, both values with an rms of around 50–100 K. The smaller structures in the equatorial regions appear consistently warmer than these larger features and have $\Delta T \approx 350 \pm 50$ K. Although the calcium line provides a less detailed surface temperature reconstruction than the iron line due to its intrinsically broader local line profile, there is reasonable good agreement between the respective Fe and the Ca maps. We thus conclude that even the weaker equatorial features are needed by the data and are thus likely real.

Several weak warm features with a contrast of $\Delta T \approx -100 \pm 50$ K are also recovered, mostly at high latitudes, but are related to dominant cool regions at similar longitudes. We attribute them to the latitudinal mirroring effect, an artifact of the Doppler-imaging technique due to the relatively high inclination value of the rotational axis of 60°.

Although the photometric data show a changing light curve for the consecutive rotation cycles (see Fig. 1), the changing spot distribution is not obvious from the spectral line profiles. To search for signs of spot evolution during the seventy nights of observation, we first reconstruct the surface temperature distribution from the entire dataset (including all photometric and spectroscopic data in Table 1). The resulting maps in Fig. 5 – one for Ca and one for Fe – are the average surface spot distributions from 3.6 consecutive stellar rotations. A simple visual comparison immediately shows that these average images are generally smoother and have lesser surface detail than the individual images in Figs. 3 and 4. Because the phase coverage is already excellent even for the individual images, we exclude a numerical reason due to the larger number of spectra (it would have the opposite effect than is observed, i.e. with more spectra the features should become better defined). We take this as evidence for spot evolution during the full 3.6 rotation cycles.

Figure 6 shows the spot changes as a function of time by simply plotting the difference between the individual images (SSi) and the average image as consecutive differential maps (the top six panels are for the differential Ca maps, the middle six panels for the differential Fe maps, and the bottom panels for the average Ca and Fe maps). Notice that the temperature range in these maps is different to the maps in the previous figures. Further evaluation is then done by using the reconstructed average map as the input map in the forward problem and generate an artificial data set, which is then compared with the observations of the individual data sets. By determining and comparing the goodness of the line-profile fits from the individual inverse solutions with the forward computations from the average map, we find that the individual solutions fit the data on average 22% better than the average image. Table 4 summarizes our goodness of fit statistics. We calculated a (pseudo) χ^2 value for all of our spectra fitted by either the maps shown in Fig. 4 or the grand-average maps shown in Fig. 5, defined as

$$\chi^2 = \sum_j \frac{(M_j - D_j)^2}{\sigma_j^2} \qquad (2)$$

with $\sigma_j = 3/[(C - D_j) * \mathrm{SNR}]$, where $C(\equiv 1)$ is the continuum level, M_j and D_j are the model and the observed datapoints, respectively, while SNR is the signal-to-noise ratio of the given spectrum. In Table 4 $\bar{\chi}^2_{\rm sub}$, which is the mean of the χ^2 values obtained for a group of spectra forming the ith subdata set SSi, is compared to $\bar{\chi}^2_{\rm avr}$, the mean value of the χ^2 values obtained for the same subdata set fitted by the grand-average map. We find that the subdatasets are generally better fitted than the average map. Note that in Table 4 there is only one case when the average map provides a slightly (4%) better fit (for the Ca-SS6 subset). We believe this exception is the result of the poor phase coverage of the photometry for this particular data set. Generally, a photometric weight of 0.1–0.2 relative to a line profile is applied, depending upon the quality of the photometric data.

At this point, we note that the main spotted regions in the average Doppler maps were also recovered by a fit to the photometric data alone (Sect. 3). The best fit to the light and color curves was achieved with a spot temperature contrast of 600±100 K, in agreement with the temperatures from the Doppler images. The photometric solution also agrees with the Doppler maps in the sense that no spots were recovered above +60° latitude. However, the spot at a longitude of ≈240° (SPOT 3 in Fig. 2) was reconstructed at a latitude higher by ≈25° than in the Doppler maps. We attribute this difference to the combined effect of sparse sampling of the consecutive light curves and the mathematical ambiguity that arises from the inversion of a disk-integrated one-dimensional data set into a surface map. Being aware of this intrinsic latitude

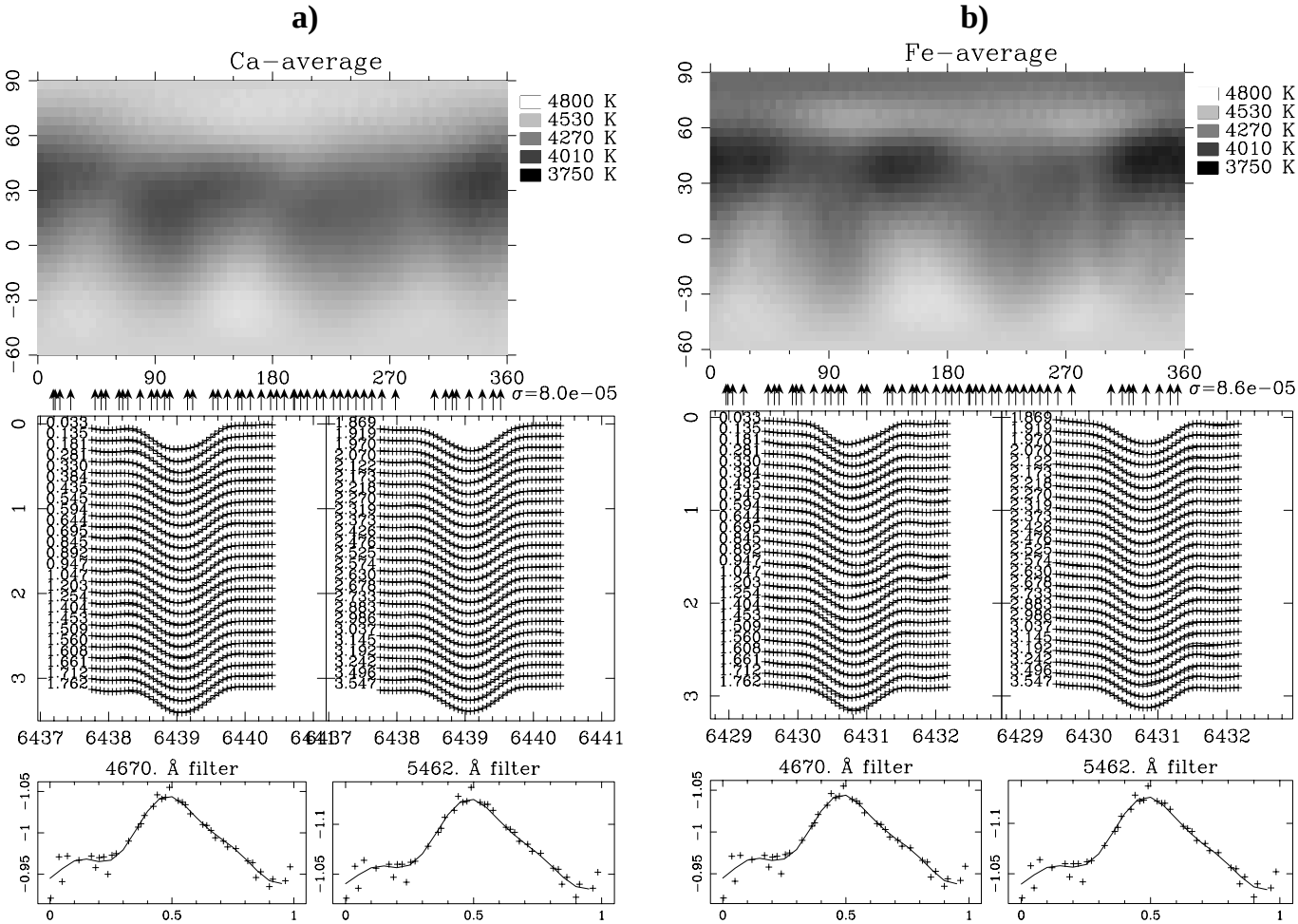

Fig. 5. a) Average Ca I-6439 map, and **b)** average Fe I-6430 map. Both maps were obtained from the entire data set spanning 3.6 stellar rotations.

Table 4. A comparison of the $\bar{\chi}^2$ values for the fits to the subdata sets by the individual images ($\bar{\chi}^2_{\rm sub}$) and by the average map ($\bar{\chi}^2_{\rm avr}$).

Ca I-6439	SS1	SS2	SS3	SS4	SS5	SS6
$\bar{\chi}^2_{\rm sub}$	4.492	5.262	5.483	3.976	2.772	3.483
$\bar{\chi}^2_{\rm avr}$	5.747	6.206	7.103	4.735	3.312	3.331

Fe I-6430	SS1	SS2	SS3	SS4	SS5	SS6
$\bar{\chi}^2_{\rm sub}$	3.575	2.981	3.822	3.699	2.886	4.804
$\bar{\chi}^2_{\rm avr}$	4.608	4.473	5.252	3.968	3.300	5.363

ambiguity, we nevertheless conclude that the *time-series analysis* of light curves is a very useful tool for studying starspot and is supportive of the Doppler-imaging results.

4.5. Differential surface rotation and spot evolution

To isolate a possible surface migration pattern and to obtain a quantitative description of it, we first cross correlate the consecutive Doppler images with each other but for both lines separately (for a detailed description of the method see Collier Cameron (2001) and previous papers in this series). We only cross-correlate the *phase independent* contiguous images, i.e., Corr{SS1/SS3}, Corr{SS2/SS4}, Corr{SS3/SS5}, and Corr{SS4/SS6} so that any cross-talk from a signature in the same line profile is excluded. This restricts the time resolution to one stellar rotation. The resulting cross-correlation-function maps (ccf-maps) for the Ca and Fe lines are displayed in Figs. 7a and b, respectively.

In most cases a coherent latitude dependency of the correlation signal is seen in maps from both spectral lines. Nevertheless, the results in Fig. 7 are inconclusive. Clear equatorial deceleration within an approximately ±30° range around the equator is seen in Corr{SS2/SS4} and Corr{SS3/SS5}, no convincing pattern seems to be evident in Corr{SS4/SS6}, and Corr{SS1/SS3} recovers a pattern with a longitudinal shift direction that appears mostly reversed with respect to the other three correlation maps in Fig. 7. We also cross-correlated the two images with the largest time span in between, i.e. Corr{SS1/SS6}, but the ambiguity remained.

We then computed an average cross-correlation function from all individual ccfs shown in Fig. 7 and

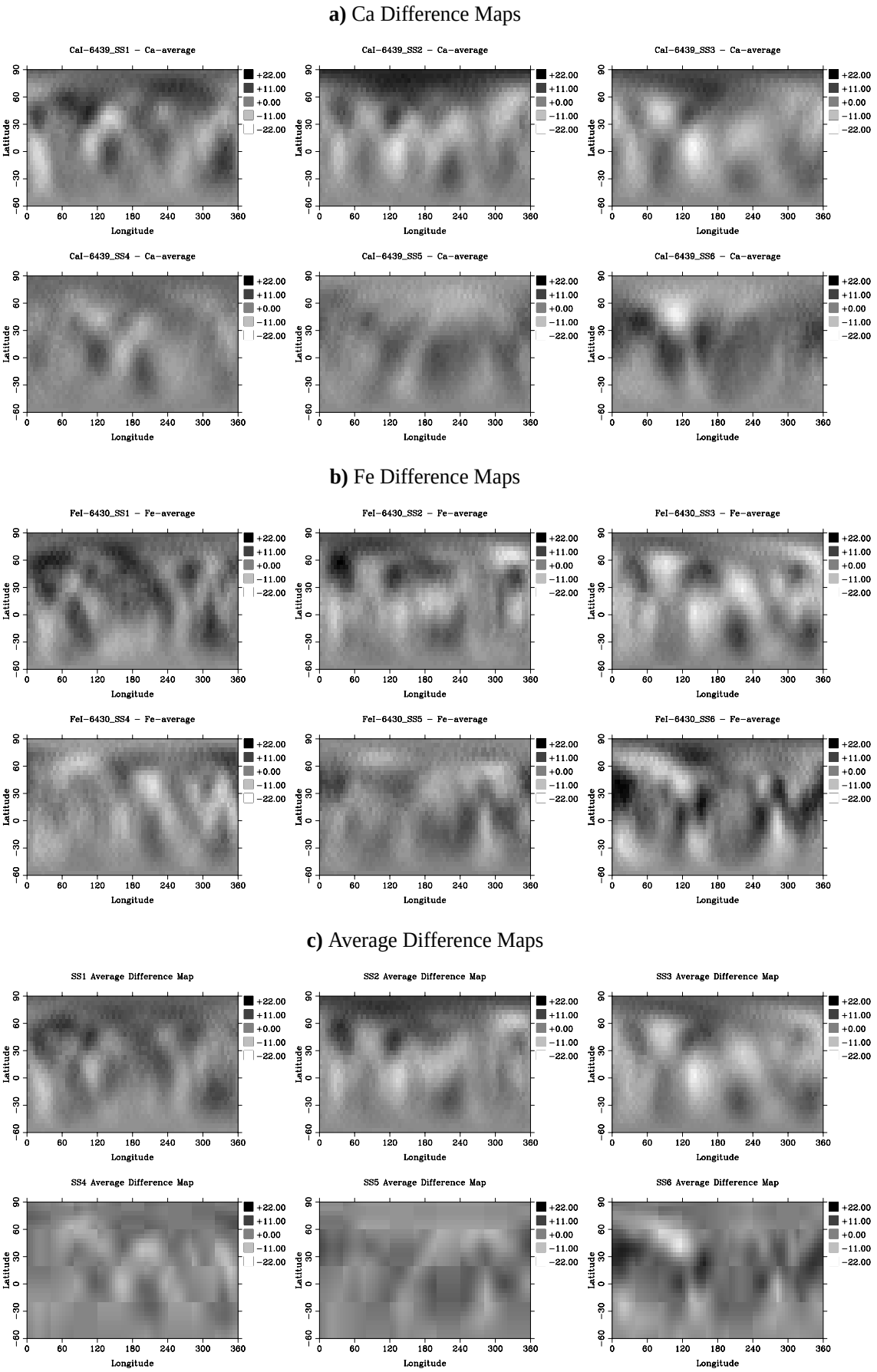

Fig. 6. Differential maps. Each map is the difference between an individual map in Figs. 3 and 4 and the averge map from Fig. 5. **a)** for calcium, **b)** for iron, and **c)** for the average calcium and iron maps.

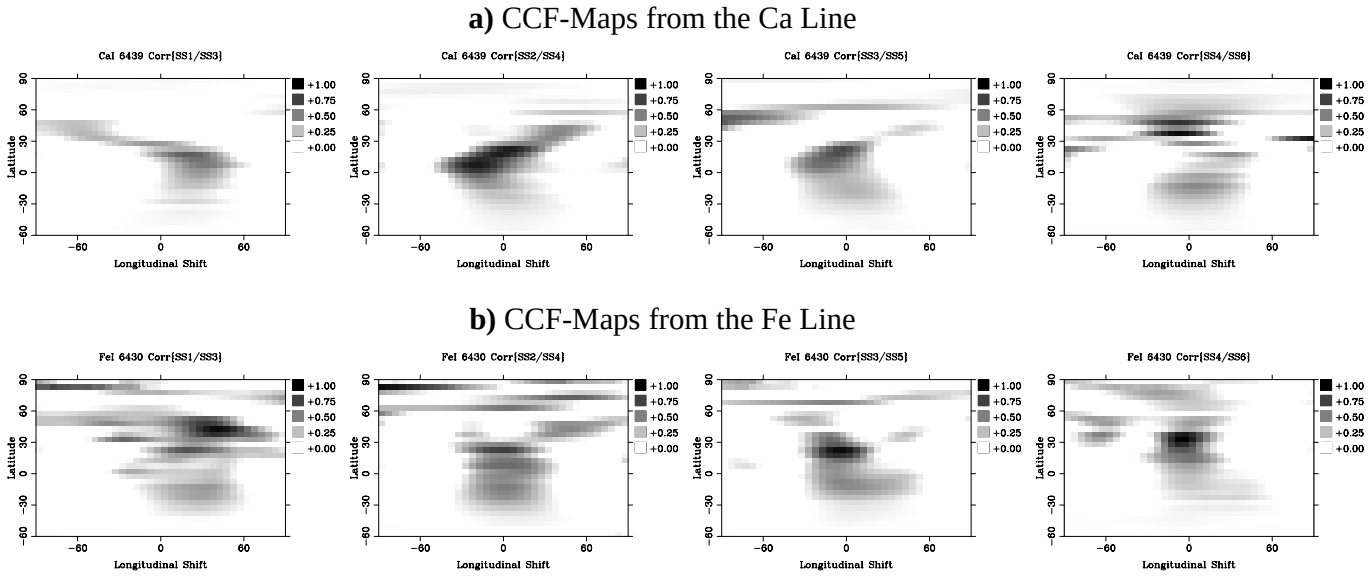

Fig. 7. The cross-correlation functions (ccf) from the independent contiguous Doppler images. **a)** displays the ccf-maps from the Ca line and **b)** those from the Fe line. The x-axis plots the longitudinal shifts in degrees. The correlation coefficient (grey scale) is weighted by the difference of the average temperature per latitude strip to the effective temperature.

searched for a correlation peak in each latitude strip (for a description of the procedure see e.g. Paper V by Weber & Strassmeier 1998). These peaks are then fitted with a bi-quadratic differential rotation law between the $[-30°, +70°]$ latitude range (i.e. the most reliable part of our Doppler maps). Despite the very weak statistical significance, it suggests a solar-like acceleration in two nearly symmetric bands around the equator for σ Gem (the χ^2 for the bi-quadratic fit was 9.31 and 10.22 was achieved for a quadratic fit with just one term, while we got 17.55 for a linear fit, i.e. the same longitudinal shift for all latitudes). Nevertheless, we consider this as too weak a detection. Obviously, a simple interpretation with a latitude-dependent surface differential rotation pattern is not straightforward from our data. We believe our analysis is hampered by two facts. Firstly, the spot pattern may not have changed enough during the time of our observations in order to resolve a coherent differential-rotation signature and, secondly, the cross correlations may have been masked by individual spot evolution.

5. Summary and conclusions

We obtained the surface temperature distribution on the RS CVn-type star σ Gem and monitored its changes over a 70-day long observing period (3.6 stellar rotations) in November 1996 – January 1997. The photometric data were subjected to a separate time-series analysis but were also used as additional constraint for the line-profile analysis. Our final conclusions are based on the combined use of the line-profiles and the continuum data.

Neither the calcium maps nor the iron maps showed high latitude spots or even a polar spot, in agreement with the earlier Doppler image published by Hatzes (1993) from 1991/92. σ Gem is not the only Doppler mapped K giant without a polar spot. Recent maps of RS CVn binaries with comparable rotation periods and spectral types also did not show polar spots, e.g. for IM Peg (K2III, P = 24.6 days), HK Lac (K0III, P = 24.4 days), and HD 208472 (G8III, P = 22.4 days) while prominent polar and/or very high-latitude spots were found on others, e.g. on XX Tri (K0III, P = 24.0 days), IL Hya (K0III-IV, P = 12.7 days), HU Vir (K0III-IV, P = 10.4 days), and YY Men (K2III, P = 9.5 days) (for references to all Doppler images published so far see Strassmeier 2001[1]). These divergent observations are a problem for the explanation of polar spots with a model that describes the deflection of rising magnetic flux tubes mostly due to the Coriolis force (Schüssler & Solanki 1992). A way out is that interior models of K giants could be vastly different for small changes in mass and, partly alternatively, the flux tubes may find an equilibrium position within the star and do not surface (Schüssler et al. 2001) which would jeopardize any meaningful comparison between observations and theory. Finally, magnetic flux tubes in binary systems may surface at preferred longitudes and latitudes and thus may bias the direct comparison (see Holzwarth & Schüssler 2000).

On the basis of the Fe I-6430 line, which provides higher surface resolution than the intrinsically broader Ca I-6439 line, we recovered several individual spots and found evidence for spot changes on times scales at least as short as one stellar rotation, if not shorter. The cross-correlation maps from one rotation to the next suggest the presence of differentially rotating latitude belts, however, the spot changes were strongly affecting the individual ccf maps and no conclusive detection is made.

[1] A complete list of Doppler images of late-type stars is maintained at `www.aip.de/groups/activity`.

Hatzes (1993) observed a spot distribution in ≈1991.9 that is very similar to ours in 1996/97 with the main difference that his spots grouped at a latitude of +55° instead of +40° as in our maps. This could be indicative for a butterfly behavior of, so far, unknown migration direction (sunspots of a new cycle appear near 35° and migrate to lower latitudes). We can only speculate what happens in between the two Doppler images but Berdyugina & Tuominen (1998) found a cycle period for σ Gem of 14.9 years from switches of active longitudes while Henry et al. (1995) found a 8.5-year period from long-term brightness variations and Strassmeier et al. (1988) claimed a period of 2.7 years from changes of the total spot area. The latitudinal spot migration in the five-year interval between Hatzes's and our maps would suggest roughly $-0.01°$/day. If so, a possible "cycle" period would be approximately 7–10 years, i.e. the time to migrate from the equator to +55° (or vice versa). The discrepancy to the photometrically determined cycle lengths is obvious, except maybe to the result from Henry et al. (1995). It is entirely possible that there is no relation between latitudinal migration rate and cycle period, though, and then, the above estimate becomes irrelevant. Sunspots can have a migration rate smaller by a factor of ten (but in a latitude range smaller by a factor of two), yet the spot cycle is longer, ≈11 years. The likely cause of such a discrepancy is that some sunspots do not migrate at all, some migrate towards the equator and still some towards the pole and all these migrations are masked by the individual spot's lifetime, the latter remains an unknown for the σ Gem spots. Our Doppler-imaging observations are only a snapshot within a (possible) cycle.

Our Ca Doppler images and the photometric time-series maps agree with each other regarding the number of active regions and their longitudinal distribution. For one spot there is a significant disagreement in the reconstructed latitudes, though. On the other hand, the agreement between the Ca maps and the Fe maps is very good, which strengthens the reliability of our conclusions regarding differential rotation and spot evolution.

Finally, a note to the detectability of differential rotation from photometry. Comparing the differential rotation parameters from the photometric spot modelling and from the Doppler-imaging analysis, we note a considerable difference of the longitudinal migration rates. For the individual features the line-profile analysis gives an average migration rate of ≈10° per stellar rotation. This value is higher by one order of magnitude than that obtained from photometry alone. The likely explanation is that the extension of the spots required by the photometric modelling is so large (50° in diameter) that the differential rotation pattern will appear significantly smeared, if not suppressed at all, and, because there is basically no latitudinal information, the observable pattern will be restricted to the latitude range covered by the reconstructed spots. Furthermore, spot modelling cannot follow the changes of a spot's shape because it is a fixed parameter. Thus, photometric spot modelling from comparably short junks of data of even relatively high precision (2.5×10^{-3} in y in our case) underestimates the effects of differential rotation by as much as one order of magnitude. A similar conclusion was reached by Lanza et al. (1994) from their Fourier analysis tests of spotted star light curves.

Acknowledgements. We wish to thank the Austrian Fond zur Förderung der wissenschaftlichen Forschung for grants S7301-AST and S7302-AST and the German Forschungsgemeinschaft for grant HU538/1. ZsK and JB thank for the financial support of the Hungarian Government through OTKA T-026165 and OTKA T-032846. JB acknowledges the Ph.D. grant of the Hungarian Soros Foundation (grant 230/2/695). The authors are grateful to Dr. K. Oláh for her kind help and useful comments on photometric spot modelling. JBR acknowledges financial support from NSERC of Canada. We also appreciate the extensive comments by an anonymous referee that led to a substantially improved version of this paper.

References

Ayres, T. R., Simon, T., & Linsky, J. L. 1984, ApJ, 279, 197
Bartus, J. 1996, Occ. Techn. Notes at Konkoly Obs., No. 1/96
Berdyugina, S. V., & Tuominen, I. 1998, A&A, 336, L25
Bopp, B. W., Dempsey, R. C., & Maniak, S. 1988, ApJS, 68, 803
Bopp, B. W., & Dempsey, R. C. 1989, PASP, 101, 516
Collier Cameron, A. 2001, in Cool Stars, Stellar Systems, and the Sun, ed. R. J. García López, R. Rebolo, & M. R. Zapatero Osorio, PASPC, 223, in press
Dempsey, R. C., Bopp, B. W., Strassmeier, K. G., et al. 1992, ApJ, 392, 187
Dümmler, R., Ilyin, I. V., & Tuominen, I. 1997, A&AS, 123, 209
Eaton, J. A. 1990, IBVS, No. 3460
Eberhard, G., & Schwarzschild, K. 1913, ApJ, 38, 292
Eker, Z. 1986, MNRAS, 221, 947
Engvold, O., Ayres, T. R., Elgarøy, Ø., et al. 1988, A&A, 192, 234
ESA 1997, The Hipparcos and Tycho catalog, ESA SP-1200
Flower, P. J. 1996, ApJ, 469, 355
Fried, R. E., Eaton, J. A., Hall, D. S., et al. 1983, Ap&SS, 93, 305
Gibson, D. M. 1980, in Close Binary Stars: Observations and Interpretations, IAU Symp. 88, ed. M. J. Plavec, D. M. Popper, & R. R. Ulrich (Reidel, Dordrecht), 31
Gray, D. F. 1992, The observation and analysis of stellar photospheres (Cambridge Univ. Press)
Hatzes, A. P. 1993, ApJ, 410, 777
Henry, G. W., Eaton, J. A., Hamer, J., & Hall, D. S. 1995, ApJS, 97, 513
Holzwarth, V., & Schüssler, M. 2000, in Poster Proceedings, IAU Symp. 200, Birth and Evolution of Binary Stars, ed. B. Reipurth, & H. Zinnecker (Potsdam, Germany), 217
Jetsu, L. 1996, A&A, 314, 153
Kővári, Zs., & Bartus, J. 1997, A&A, 323, 801
Kurucz, R. L. 1993, ATLAS-9, CD-ROM, No. 13
Lanza, A. F., Rodonò, M., & Zappalá, R. A. 1994, A&A, 290, 861
Linsky, J. L. 1984, in Cool Stars, Stellar Systems and the Sun, ed. S. L. Baliunas, & L. Hartmann (Springer, Berlin-Heidelberg), 287

Oláh, K., Panov, K. P., Pettersen, B. R., et al. 1989, A&A, 218, 192
O'Neil, D., Saar, S. H., & Neff, J. E. 1996, ApJ, 463, 766
Piskunov, N. E., & Rice, J. B. 1993, PASP, 105, 1415
Rice, J. B., & Strassmeier, K. G. 1998, A&A, 336, 972
Rice, J. B., & Strassmeier, K. G. 2000, A&AS, 147, 151
Rice, J. B., Wehlau, W. H., & Khokhlova, V. L. 1989, A&A, 208, 179
Schaller, G., Schaerer, D., Meynet, G., & Maeder, A. 1992, A&AS, 96, 269
Scarfe, C. D., Batten, A. H., & Fletcher, J. M. 1990, Publ. Dominion Astron. Obs. Victoria, 18, 21
Schüssler, M., & Solanki, S. K. 1992, A&A, 281, L69
Schüssler, M., Holzwarth, V., & Charbonnel, C. 2001, in Cool Stars, Stellar Systems, and the Sun, ed. R. J. García López, R. Rebolo, & M. R. Zapatero Osorio, PASPC, 223, in press
Singh, K. P., Slijkhuis, S., Westergaard, N. J., et al. 1987, MNRAS, 224, 481
Strassmeier, K. G. 2001, in Cool Stars, Stellar Systems, and the Sun, ed. R. J. García López, R. Rebolo, & M. R. Zapatero Osorio, PASPC, 223, 271
Strassmeier, K. G., & Bartus, J. 2000, A&A, 354, 537
Strassmeier, K. G., Bartus, J., Kővári, Zs., Weber, M., & Washuettl, A. 1998, A&A, 336, 587
Strassmeier, K. G., Boyd, L. J., Epand, D. H., & Granzer, T. 1997, PASP, 109, 697
Strassmeier, K. G., Hall, D. S., Eaton, J. A., et al. 1988, A&A, 192, 135
Strassmeier, K. G., Hall, D. S., Fekel, F. C., & Scheck, M. 1993, A&AS, 100, 173 (CABS II)
Strassmeier, K. G., Lupinek, S., Dempsey, R. C., & Rice, J. B. 1999b, A&A, 347, 212
Strassmeier, K. G., & Rice, J. B. 1998, A&A, 339, 497
Strassmeier, K. G., Serkowitsch, E., & Granzer, T. 1999a, A&AS, 140, 29
Spangler, S. R., Owen, F. N., & Hulse, R. A. 1977, AJ, 82, 989
Vogt, S. S., Hatzes, A. P., Misch, A. A., & Kürster, M. 1999, ApJS, 121, 547
Weber, M., & Strassmeier, K. G. 1998, A&A, 330, 1029
Yi, Z., Elgarøy, Ø., Engvold, O., & Westergaard, N. L. 1997, A&A, 318, 791